Experimental Mechanics (2011) 51:575–589
DOI 10.1007/s11340-010-9422-7

Multi-scale Mechanical Characterization of Palmetto Wood using Digital Image Correlation to Develop a Template for Biologically-Inspired Polymer Composites

S. Haldar · N. Gheewala · K.J. Grande-Allen · M.A. Sutton · H.A. Bruck

Received: 11 June 2010 / Accepted: 10 October 2010 / Published online: 4 December 2010
© Society for Experimental Mechanics 2010

Abstract Palmetto wood is garnering growing interest as a template for creating biologically-inspired polymer composites due to its historical use as an energy absorbing material in protective structures. In this study, quasi-static three-point bend tests have been performed to characterize the mechanical behavior of Palmetto wood. Full-field deformation measurements are obtained using Digital Image Correlation (DIC) to elucidate on the strain fields associated with the mechanical response. By analyzing strain fields at multiple length scales, it is possible to study the more homogeneous mechanical behavior at the macroscale associated with the global load-deformation response; while at the microscale the mechanical behavior is more inhomogeneous due to microstructural failure mechanisms. Thus, it was possible to determine that, despite the presence of discontinuous macro-fiber reinforcement, at the macroscale the response is associated with classical bending and progressive failure processes that are adequately described by Weibull statistics proceeding from the tensile side of the specimen. At the microscale, however, the failure mechanisms giving rise to the macroscopic response consist of both shear-dominated debonding between the fiber and matrix, and inter-fiber matrix failure due to pore collapse. These microscale mechanisms are present in both the compressive and tensile regions of the specimen, most likely due to local macro-fiber bending, which is independent of the global bending state. The pore collapse mechanism observed during mechanical loading appears to improve the energy absorption of the matrix material, thereby, transferring less energy and shear strain to the macro-fiber-matrix interface for initiation of debonding. However, the pore collapse mechanism can also accumulate substantial shear strain, which results in matrix shear cracking. Through these complex failure mechanisms, Palmetto wood exhibits a high resistance to catastrophic failure after damage initiation, an observation that can be used as inspiration for creating new polymer composite materials.

Keywords Multiscale measurement · Palmetto wood · Composite material · Digital image correlation · Hierarchically-structured material · Multiple failure mechanism · Three-point bend experiment

S. Haldar · H.A. Bruck (✉, SEM member)
Department of Mechanical Engineering, University of Maryland, College Park, MD, USA
e-mail: bruck@eng.umd.edu

N. Gheewala · K.J. Grande-Allen (SEM member)
Deparment of Bioengineering, Rice University, Houston, TX, USA

M.A. Sutton (SEM Fellow)
Deparment of Mechanical Engineering, University of South Carolina, Columbia, SC, USA

Introduction

Palmetto wood is a natural heterogeneous material with hierarchical structure that has exhibited extraordinary energy absorbing capabilities when used as a protective structure during both the Revolutionary and Civil Wars. Hierarchically-structured materials like Palmetto wood have recently drawn the attention of researchers interested in understanding how their unique structure leads to optimized properties (e.g., low density accompanied by high mechanical strength) that may serve as inspiration for development of engineered materials. Efforts have already been made to prepare biologically-inspired, synthetically-based, hierarchically-structured engineering

materials [1]. To do so, an in-depth understanding of structure-property relationships and failure mechanisms in the inspirational material is necessary. For example, assessing the microscale mechanical behavior is helpful in understanding the macro-scale fracture process in wood [2].

The unique hierarchical structure of the fibers in Palmetto wood to achieve mechanical strength and serve the biological purposes and its relationship to the mechanical behavior of the fibers has recently been characterized at multiple length scales and related to the mechanical behavior of the fibers [3]. Through the use of optical microscopy, the hierarchical structure of the Palmetto wood was established previously, as shown in Fig. 1 over length scales ranging from the scale of Palmetto tree to the scale of the microfibers within the macrofibers embedded in the porous cellulose matrix. The volume fraction of macrofibers of diameters of approximately 300–500 μm was determined to be 12% and 20% in the optically dark and light regions respectively. Gas pycnometry had been utilized to characterize the porosity in the cellulose matrix, as well as the bulk and true density of the Palmetto wood.

In this previous work, the understanding was limited to the elastic behavior and strength of the Palmetto. However, there is a need for a more advanced mechanical characterization of the inelastic behavior of Palmetto wood at multiple length scales to improve understanding of the mechanisms that give rise to its extraordinary energy absorbing capacity. Therefore, to understand the inelastic behavior of Palmetto wood, and thereby provide the foundation for developing heterogeneous materials with similar properties, appropriate mechanical characterization techniques are needed to elucidate on the deformation process at different length scales. Macro-scale measurement techniques employing point-wise contact-based methods, such as strain gauges and extensometers, are suitable for determining global deformation and loading conditions associated with a homogenized strain response. However, micro-scale deformations are typically more inhomogeneous and require more advanced techniques, such as photoelasticity and interferometric techniques. These optical measurement techniques have several key advantages over point-wise contact-based techniques; most notably they are non-contacting and allow full-field measurements and digitization for computational analysis [4].

The most popular optical measurement techniques for measuring inhomogeneous deformation fields at different length scales include interferometry-based techniques, such as Moire, holography, and speckle, as well as non-

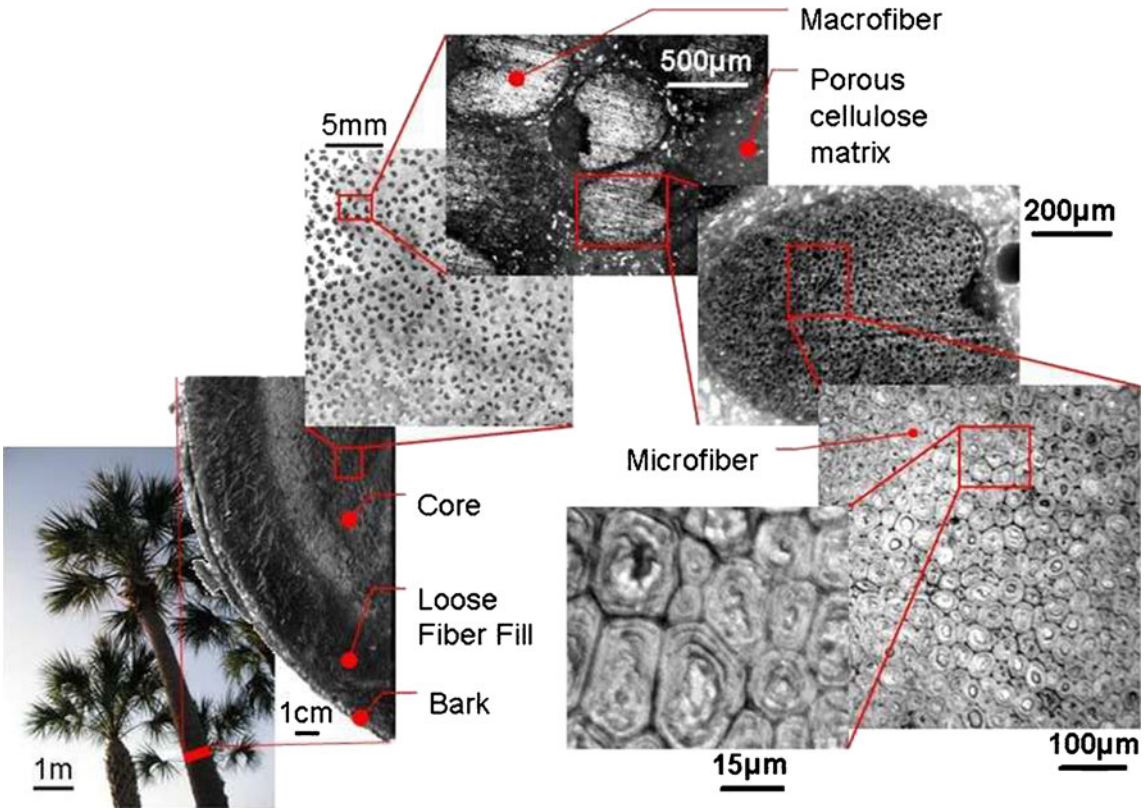

Fig. 1 Cross-section of hierarchical structure in Palmetto wood previously obtained using optical microscopy [3]

interferometric techniques like marker techniques [4, 5] and digital image correlation [6]. Moire interferometry [7–10], holographic interferometry [11, 12] and speckle interferometry [7, 8, 13–18] have been employed extensively for nanoscale and microscale deformation measurements. A major disadvantage of interferometric techniques is the level of surface preparation required to ensure reflection and interference, which can be extremely challenging for materials like Palmetto wood [19]. Marker methods have proven to be more useful for deformation measurements at multiple length scales. In these approaches, a pre-marked (by grid or dot) specimen is used for the experiments and the marks on the specimens are tracked to obtain the deformation field [20, 21].

Digital Image Correlation (DIC) is another full-field deformation measurement technique that has been successfully applied at multiple length scales. The DIC method has been widely accepted and frequently used for planar full-field deformation measurement. Since the DIC method employs both optical imaging and digital image processing, it is oftentimes considered a hybrid technique coupling optical imaging with numerical computing. DIC compares the digitized images of an undeformed (reference) specimen to multiple images of deforming specimen to yield full-field displacement and strain fields [22, 23]. DIC can be applied at the microscale and nanoscale with an appropriate speckle pattern [24]. Generally, a random speckle pattern that does not include a very high density of only high or low grey levels (well-spread) is considered appropriate for DIC. Also, DIC can be used at multiple length scales by using cameras with sufficiently high resolution.

DIC has been used for characterizing inhomogeneous deformations at different length scales in many applications. For example, it has been previously used for inter- and intra-granular deformation measurements [25]. It has also been found to be particularly suitable for strain measurement in inhomogeneous, anisotropic, non-linear materials [26]. For example, Gonzalez and Knauss [27] used the DIC technique to capture local strain inhomogeneity in a particulate composite due to an applied globally homogeneous strain. DIC has also been used to capture nonuniform deformation fields in a variety of materials including concrete [28], polymeric foam under compression [29], plastic deformation of binary aluminum alloy [30] and closed-cell aluminum alloy foam [31], among their applications. DIC has been found to be useful in strain measurement [2, 32] and fracture studies [33] in wood. For example, DIC has been used to measure strains around a knot in wood during three-point bend test [2]. In that particular case, the natural texture of wood can serve as the speckle pattern for DIC. Thus, DIC is a proven optical measurement technique for nonuniform strain analysis in materials such as wood, and would be highly suitable for the mechanical characterization of Palmetto wood at multiple length scales.

In this paper, a more detailed understanding of failure mechanisms in Palmetto wood at several length scales is investigated at multiple length scales using DIC. Testing is conducted using quasi-static three-point bending in order to characterize the microstructural failure mechanisms in a more complex stress state that can initiate multiple failure mechanisms. These measurements are then used to identify and quantify the evolution of the failure mechanisms of Palmetto wood at the microscale in order to relate them to the macroscopic response. Thus, for the first time it will be possible to understand how these failure mechanisms translate across multiple length scales in a natural hierarchically-structured material that may serve as a template for biologically-inspired polymer composites. In previous work, a model laminated composite structure inspired by Palmetto wood was reported and the effects of the bioinspired hierarchical structure on the mechanical behavior was characterized [3]. The bioinspired laminated composite exhibited higher flexural energy density and its Weibull failure statistics were enhanced and found to be closer to those of Palmetto wood.

Experimental Method

The motivation of choosing three-point bend test as a characterization technique lies in the versatility of the stress state in the specimen due to the presence of both compressive and tensile axial strains, as well as shear strain, in the specimen. Three-point bend specimens with dimensions $100\times9\times9$ mm^3 were prepared from a harvested Palmetto tree for the present study with a volume fraction of macro-fibers of 12%. Tests were performed in an Imada model MX 500 load frame [Fig. 2 (a)] with a Z2H-440 2 kN load cell that has a load resolution of 0.1 kg. The load on the specimen was obtained using the load cell attached to the base of the three-point bend test fixture, while vertical displacement of the load point was determined using a dial caliper attached to the load cell with a displacement resolution of 10 microns. Supports for the three-point bend test fixture were 62.5 mm apart, and the specimen was loaded in two different optical configurations: (1) images acquired of the central region of the specimen for macro-scale tests, and (2) images acquired focusing on region near the central loading point of the specimen for microscale tests. The specimen was loaded with the fibers oriented transverse to the loading direction. Quasi-static bending was performed under displacement control at a macro-scale flexural strain rate 1.6×10^{-4}/sec.

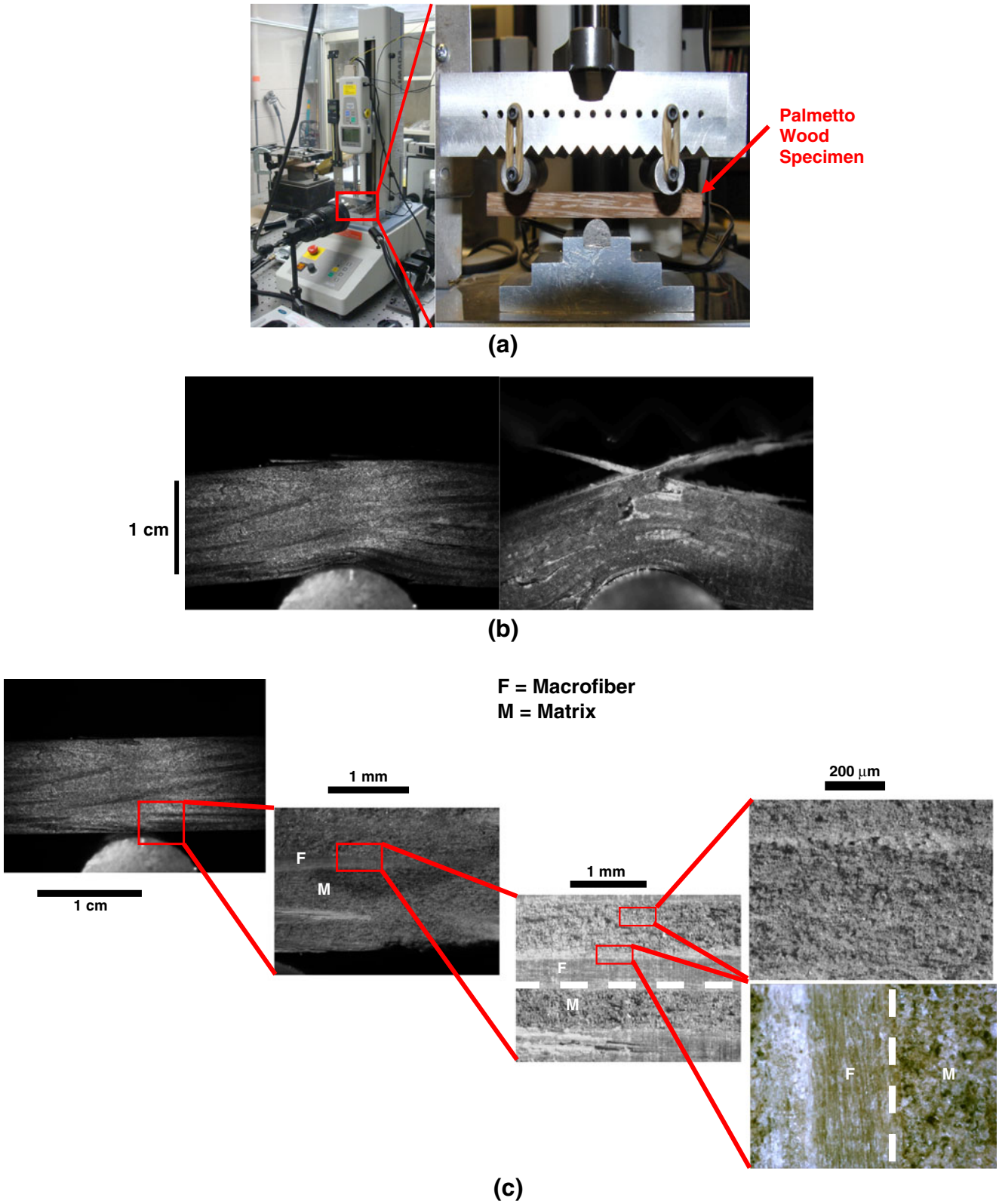

Fig. 2 (**a**) Three-point bend test set up and specimen configuration used to characterize the deformation of Palmetto wood at multiple length scales, and (**b**) Images of deformed Palmetto wood in three-point bending. The natural texture of the wood was determined to be sufficient for DIC analysis (**c**) Fields of view at several magnifications demonstrating the multiscale deformation measurement methodology where the interface is denoted by a dashed line and the matrix and macrofiber by M and F, respectively. The images are of different specimens that were sequentially tested at several magnifications

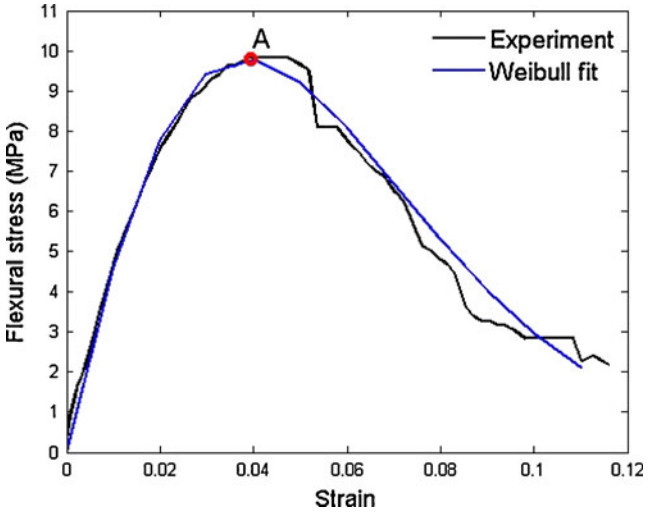

Fig. 3 Representative quasi-static macroscopic flexural-stress strain curve for Palmetto wood with a Weibull fit indicating that the failure response conforms to a Weibull distribution

The Palmetto wood surface texture was good enough for texture image correlation at all length scales, which obviated the need to apply an artificial speckle pattern. A Flea 2 digital camera (Point Grey Research, Richmond, BC, Canada) with 2.0 Megapixel resolution was used to capture the images of specimen during the test with a very high signal-to-noise ratio. The specimen surface was illuminated by a MI-150 high intensity fiber optic illuminator from Edmund Optics (Barrington, NJ, USA). The specimen and its failure under three-point bend test are shown in Fig. 2 (b). The DIC analysis was performed using a commercially available software Vic-2D from Correlation Solutions Inc. (Columbia, SC, USA).

Tests were performed sequentially and repeatedly on different samples at several magnifications in order to reliably measure deformations at multiple length scales. The fields of view at multiple length scales are depicted in Fig. 2(c). The images demonstrate the multiscale measurement methodology. In these images, M and F indicate porous cellulose matrix and macrofiber respectively while the interface is denoted by a dashed line. As mentioned earlier, the tests were performed on different specimens and the images only show the relative magnifications at which the deformation measurements were performed. The smallest subset size compatible with the surface texture of the image was used for image correlation.

Experimental Results

Deformation Measurement at Macro-Scale

Representative flexural stress-strain response of the Palmetto wood specimen in three-point bending and the fit of a Weibull distribution for the failure response of a bundle of fibers are depicted in Fig. 3 [3]. As a first order approximation, the flexural stress, flexural strain and strain energy for a specimen with cross-section 9.5×9.5 mm^2 and support span length of 62.5 mm are calculated using the classical relations for homogeneous isotropic materials given by:

$$\sigma = \frac{3PL}{2bh^2}, \varepsilon = \frac{6\delta h}{L^2}, U = \int_0^{\varepsilon} \sigma \, d\varepsilon' \tag{1}$$

where P is the applied load, L is the support span, b is specimen thickness, h is specimen height, and δ is the deflection. For these specimen dimensions, the cross-sectional area is nearly 400 times the cross-sectional area of an individual fiber in the macro-fiber bundle, so the global behavior should be considered macroscopic. The bulk flexural modulus of this representative specimen was determined to be approximately 500 MPa, and the specimen failed at 4% elongation with a corresponding nominal stress of about 10 MPa. The Weibull distribution of the failure response for a bundle of fibers is given by:

$$\sigma = E\varepsilon \ \exp\left[-\left(\frac{\varepsilon}{\varepsilon_0}\right)^{\beta}\right], \tag{2}$$

where ε_0 and β are the Weibull parameters and E is elastic modulus. The Weibull parameters are chosen as ε_0=0.05, β=1.5 with elastic modulus (E) as 500 MPa [3]. The strain energy up to the failure initiation has been determined to be 3.0 J/cm^2.

Representative displacement and strain fields obtained using DIC at the macro-scale can be seen in Fig. 4 before the onset of failure. The specimen in the image was 500 pixels in height, and DIC was performed using a subset size of 25×25 pixel^2 (0.45×0.45 mm^2) for image correlation. As can be noted from Fig. 3, the specimen can bear substantial load after failure initiation and does not exhibit catastrophic failure and absorbs significant amount of strain energy during the multi-step failure response, a response that is preferred for engineering applications where energy absorption is important. Indeed, it was noted in a previous study that fiber-bridging is the primary mechanism for Palmetto wood to carry load post-failure [3]. The displacement and strain fields shown in Fig. 4 correspond to point A in the flexural stress-strain response of the specimen (Fig. 3). The macroscopic displacement field is symmetric with respect to the loading point indicating that at the macroscopic scale, the behavior of the wood appears to be homogeneous. However, the accompanying macro-scale strain fields reveal a slight asymmetry with respect to the loading point that may arise due to inhomogeneity from the macro-fiber distribution in the wood along the specimen length.

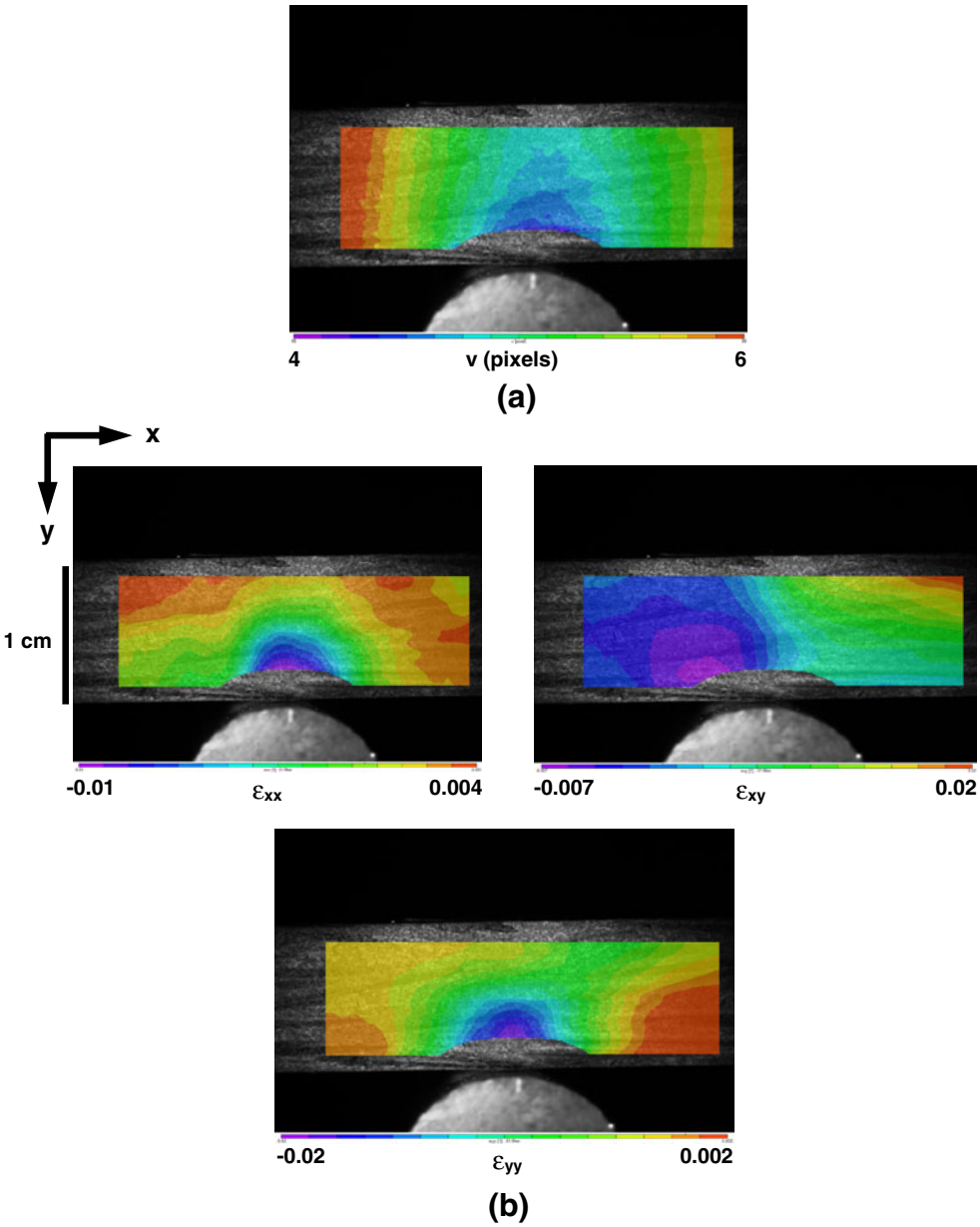

Fig. 4 Macroscopic (**a**) displacement (pixels) and (**b**) strain fields in Palmetto wood obtained under three-point bending before the onset of failure. The fields evidence macroscopically inhomogeneous behavior of the material. The load level corresponds to point A of Fig. 3

The bending response of the specimen was evaluated through the classical beam bending theory for homogeneous isotropic material. The vertical displacement along the length of the specimen is extracted from the DIC analysis as shown in Fig. 5. The displacement field appears to be similar to that expected from three-point bending of a homogeneous isotropic material. The flexural strain is calculated from the curvature-strain relationship in the beam bending of homogeneous isotropic material through a quadratic fit to the displacement. The strain is determined to be 0.007, which matches well with the axial strain of 0.006 directly obtained from the DIC displacement field in the tensile region of the specimen. Thus, it can be concluded at this length scale that the behavior of the specimen is primarily homogeneous, although there can be some slight asymmetry in the displacement due to the distribution of macro-fibers.

The degraded modulus of Palmetto wood was also determined by flexural unloading and reloading to evaluate the nature of the damage evolution. The variation of the degraded modulus normalized by initial modulus with the maximum elastic curvature of the specimen, evaluated both from theoretical calculations and experimental measurements, is shown in Fig. 6 (a), and both the results match well. The damage variable (D) based on the elastic energy equivalence given by $D = 1 - (E/E_0)^{1/2}$ has been determined, and regression fit using the progressive damage evolution formula given by $D = D_{\lim}\{1 - \exp[-a(\varepsilon - \varepsilon_i)]\}$ is shown in Fig. 6 (b) [34]. The parameters of the

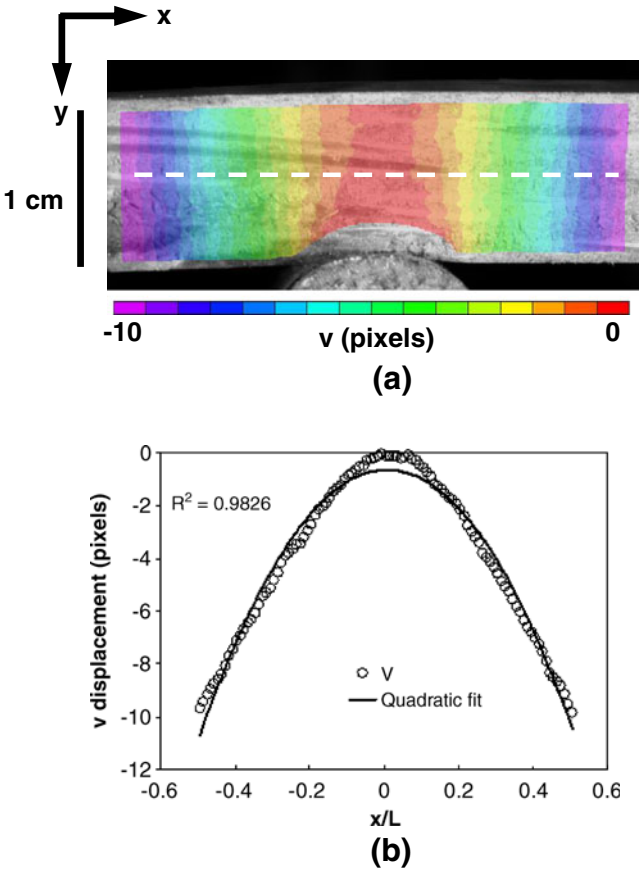

Fig. 5 (**a**) Vertical displacement field of the Palmetto wood specimen under quasi-static three-point bend test that resembles typical displacement field in three-point bending for homogeneous isotropic material, (**b**) vertical displacement of the specimen along the line (shown in (**a**)) and quadratic fit used to calculate the strain from beam bending theory

progressive damage evolution are the upper bound limit for material damage, $D_{lim}=0.9$, threshold strain for damage initiation $\varepsilon_i=0.034$, acceleration factor of damage evolution $a=20$.

Deformation Measurement at Microscale Within Elastic Regime

Since Palmetto wood is a hierarchically structured material over several length scales, images were taken at multiple magnifications to elucidate the roles of the porous cellulose matrix and embedded fibers in the failure process. Images were captured at magnifications that were 10X higher than the macro-scale to better quantify the mechanical behavior of the Palmetto wood at what is considered to be the intermediate microscale.

At this magnification, the macrofibers are 70–75 pixels wide and separated by approximately 140–150 pixels at 20% volume fraction, so a subset size of 50×50 pixel^2 (0.11×0.11 mm^2) was used for image correlation. Spatially cyclic strain distribution along the depth (vertical direction) consistent with the fiber distribution starts to become evident at this magnification (Fig. 7) and high shear strain between fibers can be more easily discerned as shown in Fig. 7 (b). The images are acquired at the compressive side of the specimen approximately 2 mm from the central support at the bottom side of the specimen. The load level corresponds to a flexural stress of 1.4 MPa and flexural strain of 0.2%, values that are well below the level required for failure initiation. The strain field is consistent with a highly inhomogeneous material response, with localized strain that can lead to fiber-matrix debonding or matrix failure. It can be noted in the strain fields from higher magnification images that the material is prone to shear debonding at the macro-fiber-matrix interface and within the cellulose matrix, more due to the high shear strain accumulation than to the tensile failure of the macro-fiber. Furthermore, there is significant localization of normal strain in between the fibers within the matrix that could

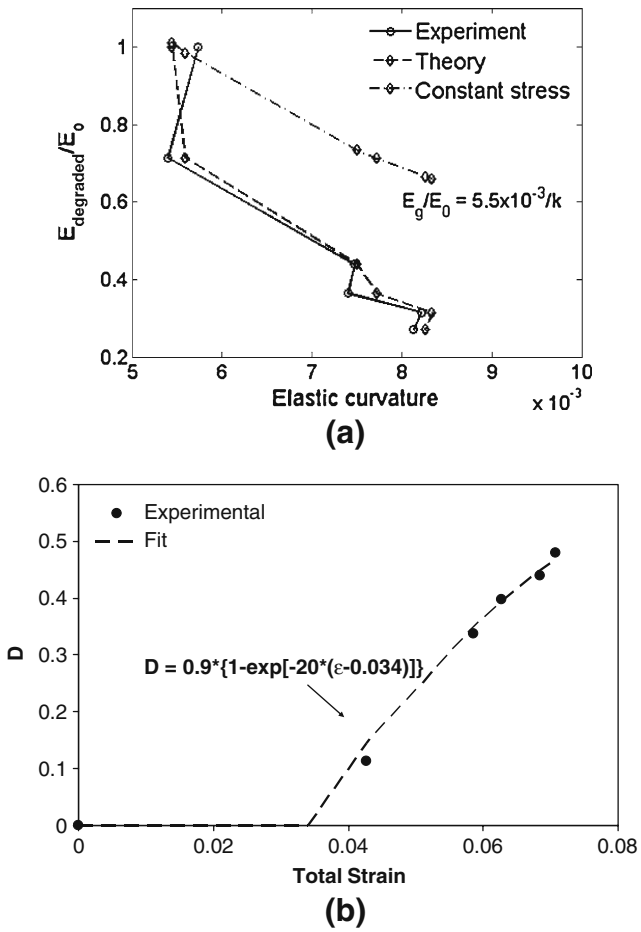

Fig. 6 (**a**) The comparison of theoretical calculated and experimental measured maximum elastic curvatures with respect to normalized degraded modulus and the upper bound for constant stress, and (**b**) evolution of the elastic energy equivalent damage, D, with total strain along with a fit using the formula for progressive damage evolution

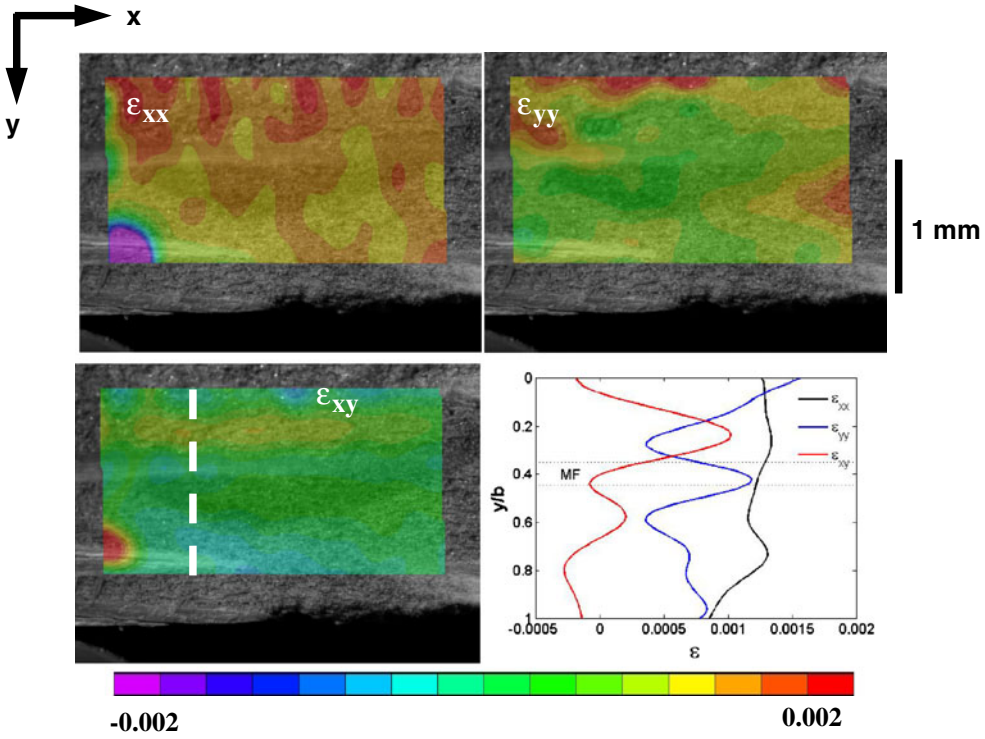

Fig. 7 Strain contours in Palmetto wood during three-point bending obtained in compression region of specimen at intermediate microscale magnification exhibiting more inhomogeneous shear strain distribution consistent with the porous microstructure of the matrix, and strain distribution along the depth (along *white dashed line*). The shear strain and transverse normal strain varies cyclically with macro-fiber (MF) and matrix distribution

potentially lead to pore collapse (i. e., collapse of cellular structure) and densification of the microstructure into layers (i.e., stratification) as typically seen in ductile, porous materials.

Images were also captured on the tensile side (i.e., top side of the specimen) at a distance of approximately 5 mm from the center support to elucidate the tensile strain distribution. However, strain analysis on the tensile side

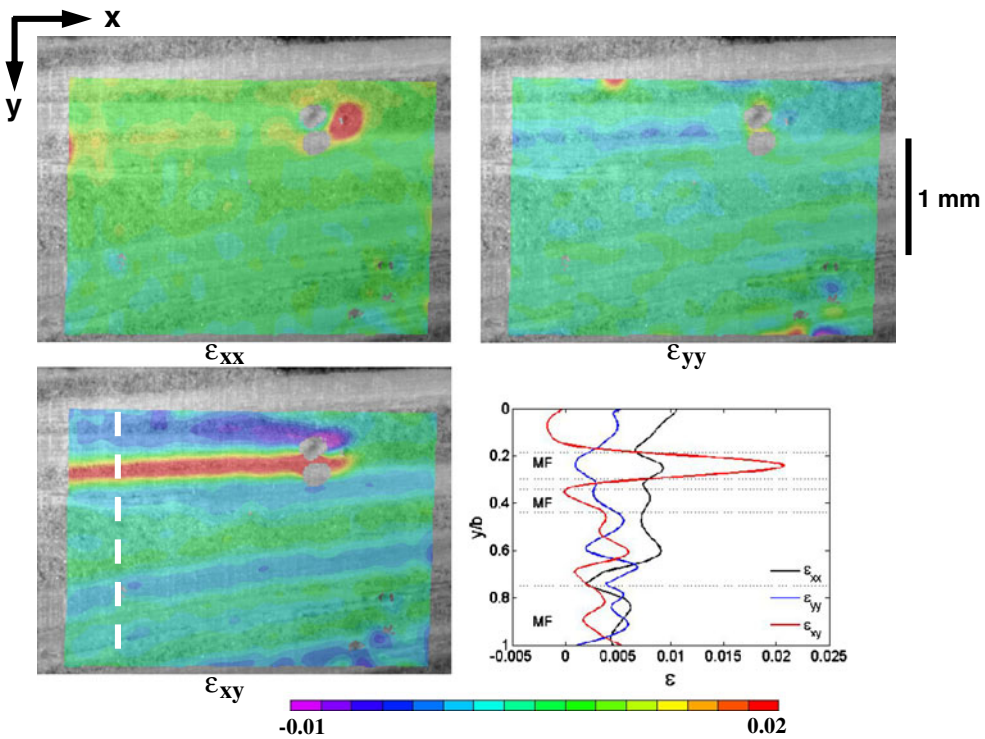

Fig. 8 Strain contours in Palmetto wood during three-point bending in tensile region of the specimen at intermediate microscale magnification, and strain distribution along the depth (*dashed white line*) with similar variability due to microstructure as observed in compression region. Any variability in strain magnitude between compressive and tensile regions is attributed to differences in the macro-fiber distribution

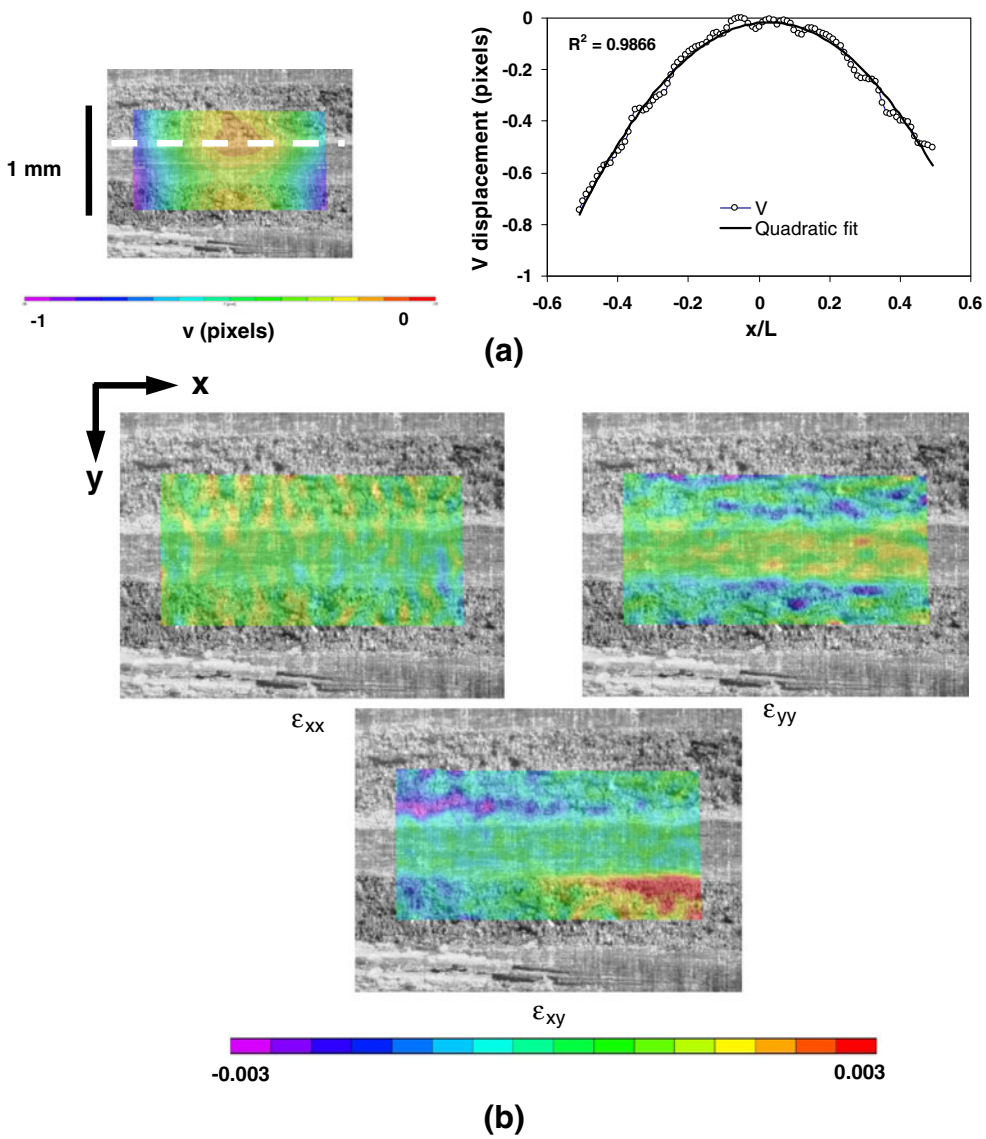

Fig. 9 (**a**) Local bending of macro-fiber (*dashed white line* indicates the fiber-matrix interface) (**b**) Strain fields in Palmetto wood at second intermediate microscale obtained near fiber-matrix interface

of the specimen revealed that the strain distribution at the macro-fiber-matrix interface remains the same as was observed on compression side at the microscale, as shown in Fig. 8. High shear strain is noted at the macro-fiber-matrix interface and the strains vary cyclically with the local distribution of the macro-fiber and cellulose matrix. It is noted that there is a minor difference between the strain distributions in the tensile and compressive regions which might be due to variability in the macro-fiber distribution within the Palmetto wood. Nevertheless, the basic micro-structural response is found to be similar. Thus, the high shear strain at the macro-fiber-matrix interface and similarity in strain distribution is established irrespective of the global deformation state in either the tensile or compressive regions of the specimen.

Microscale strain measurements shown in Fig. 9 and obtained when imaging at a higher magnification, indicate substantially higher strain at the matrix-macro-fiber interface than within the macro-fiber. In fact, the strain in the fiber is an order of magnitude smaller due to the higher rigidity of the fiber. The strain fields are shown for a flexural stress of approximately 2.1 MPa and a global flexural strain of 0.3% flexural strain, which is in the nominally elastic regime. The displacement field in the specimen, the vertical displacement profile and strain distributions are shown in Fig. 9 (a) and (b). The bending appears qualitatively similar to the classical bending of a stiff fiber in a compliant matrix, however with the caveat of asymmetry along the fiber. The asymmetry might occur due to inhomogeneity in matrix stiffness. The curvature of the macro-fiber in local bending at the microscale is used to calculate microscale strain level, and is consistent with the axial strain of 0.003 measured from the microscale DIC displacement fields. The curvature of the specimen at the macro-scale and that of the macro-fiber at the microscale are found to be approximately similar at equivalent macro-

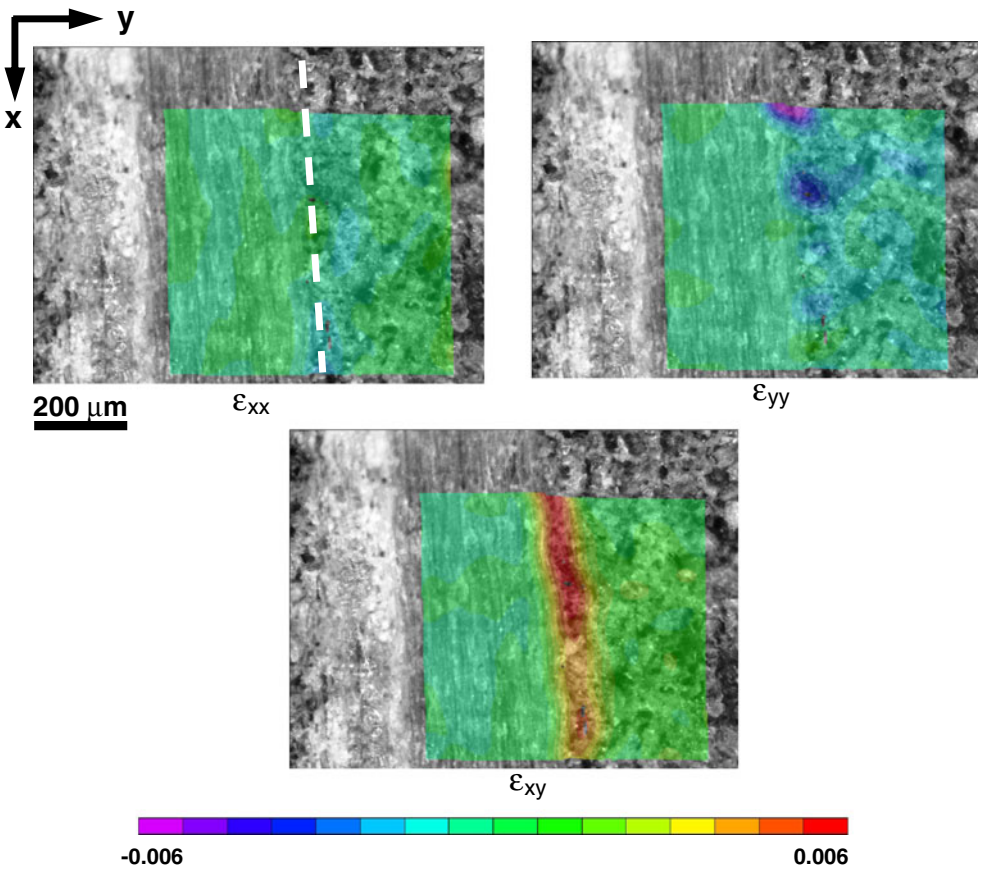

Fig. 10 Strains measured 200 μm into matrix at micro-scale indicating concentration of shear strains very close (~0.25d_f) to the fiber-matrix interface with associated pore collapse which may allow the shear strain to build up at the interface (*dashed white line*)

scale flexural strain level, which is approximately 0.001 mm^{-1}. Thus, the flexural response translates from the macro-scale to the microscale through the mechanical behavior of the macro-fiber rather than through the porous cellulose matrix. However, a positive transverse strain occurs in the fiber that might result from the debonding of microfibers within the macro-fiber due to local bending of the macro-fiber as depicted in Fig. 9 (a).

High interfacial shear strain makes the material prone to debonding. The strain fields in the fibers were more homogeneous and smaller in magnitude as compared to that in the matrix. This difference is not unexpected, since the mechanical properties of the macro-fiber such as stiffness are greater than those of the porous cellulose matrix, and therefore the response is nearly rigid. To better elucidate the interfacial strain distribution, images were captured at 20X magnification. A subset size of 35×35 $pixel^2$ (0.028×0.028 mm^2) was used for image correlation. The strain fields in Fig. 10 help to understand the difference in strain level in macro-fiber and matrix. The strain fields indicate high shear strain at the macro-fiber-matrix interface and the normal strains are found to be much higher in the matrix. However, the interfacial mechanics were found to be the same as elucidated at the lower magnification, except the high shear strain and compressive strain associated with pore collapse is more clearly evident in the matrix at the interface using higher magnification.

Deformation Measurement at Microscale Within Failure Regime

To understand failure initiation, the strain field was evaluated from the images captured just after the maximum stress level had been reached (Fig. 11). The global stress strain behavior obtained from homogeneous isotropic assumption is shown. Comparing the strain fields obtained at the microscale with observations of failure initiation in the images [Fig. 11 (a), (b)], it would appear that crack initiation within the cellulose matrix is dominated by shear strain. The strain field in the pre-failure image can be used to predict the failure initiation. The images correspond to a global flexural stress of 11 MPa and flexural strain of 3%. As can be noted from the strain fields, the shear strain at the failure initiation site is much higher (6%) than the normal strains (1%).

The process of shear cracking in the matrix was evaluated at the highest magnification level of 20X from the macro length scale. While debonding takes place in the matrix-fiber interface due to shear strain, compressive failure at the micro-scale level is noted (Fig. 12) due to

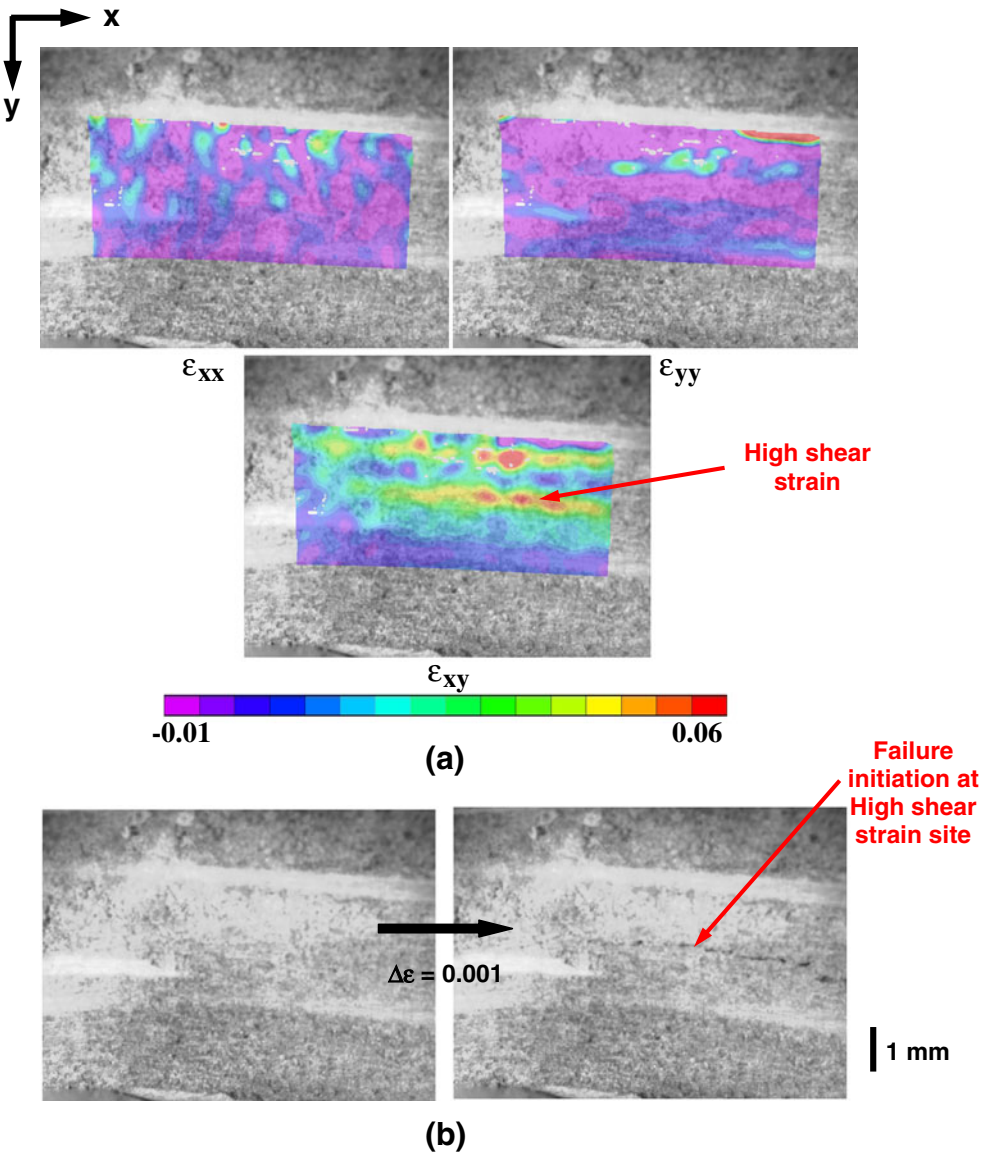

Fig. 11 (**a**) Strain fields in the Palmetto wood specimen under quasi-static three-point bend before failure initiation and (**b**) failure initiation by shear cracking in the cellulose matrix after a macro-scale flexural strain increment, $\Delta\varepsilon$, of 0.001. The failure initiation corresponds to the high shear strain site

pore collapse (i.e., crushing) of the matrix. At lower global strain levels, the matrix begins to undergo localized compressive strain and shear strain at discrete locations. However, as the global strain increases these strains begin to coalesce into a band due to pore collapse, and a shear crack begins to form as evidenced by the high levels of shear strain along this band. The evolution of shear cracking can be seen in Fig. 12.

Figure 12 demonstrates that compressive failure grows faster than the tensile failure site, leading to a macro-crack. Also, it is noted that higher compressive strain is accumulated faster than the shear strain, as indicated by the second strain contours in Fig. 12, where compressive strain reaches 0.09% while shear strain is approximately 0.06%. The compressive strain was also evidenced to some extent in larger length scale deformation measurements as shown in Fig. 10. The collapse of the porous matrix increases the local shear strain which generates potential sites for the initiation of shear cracks as the global strain increases. Hence, it is believed that the pore collapse mechanism leads to shear accumulation. Furthermore, it is most likely the mechanism by which the flexural response can translate uniformly from the macro-scale to the microscale in the macro-fiber, as was previously discussed.

To map the microscopic-to-macroscopic behavior of the Palmetto wood, the strains at each length scale were compared. The evolution of microscale local strains obtained by DIC from the 10X magnification images captured on the tensile and compressive side of the specimen are tracked over the quasi-static bending process with respect to the macro-scale flexural strain. The evolution is depicted in Fig. 13. The microscale strains are found to increase steadily with the macro-scale flexural strain. The microscale transverse and shear strain increased

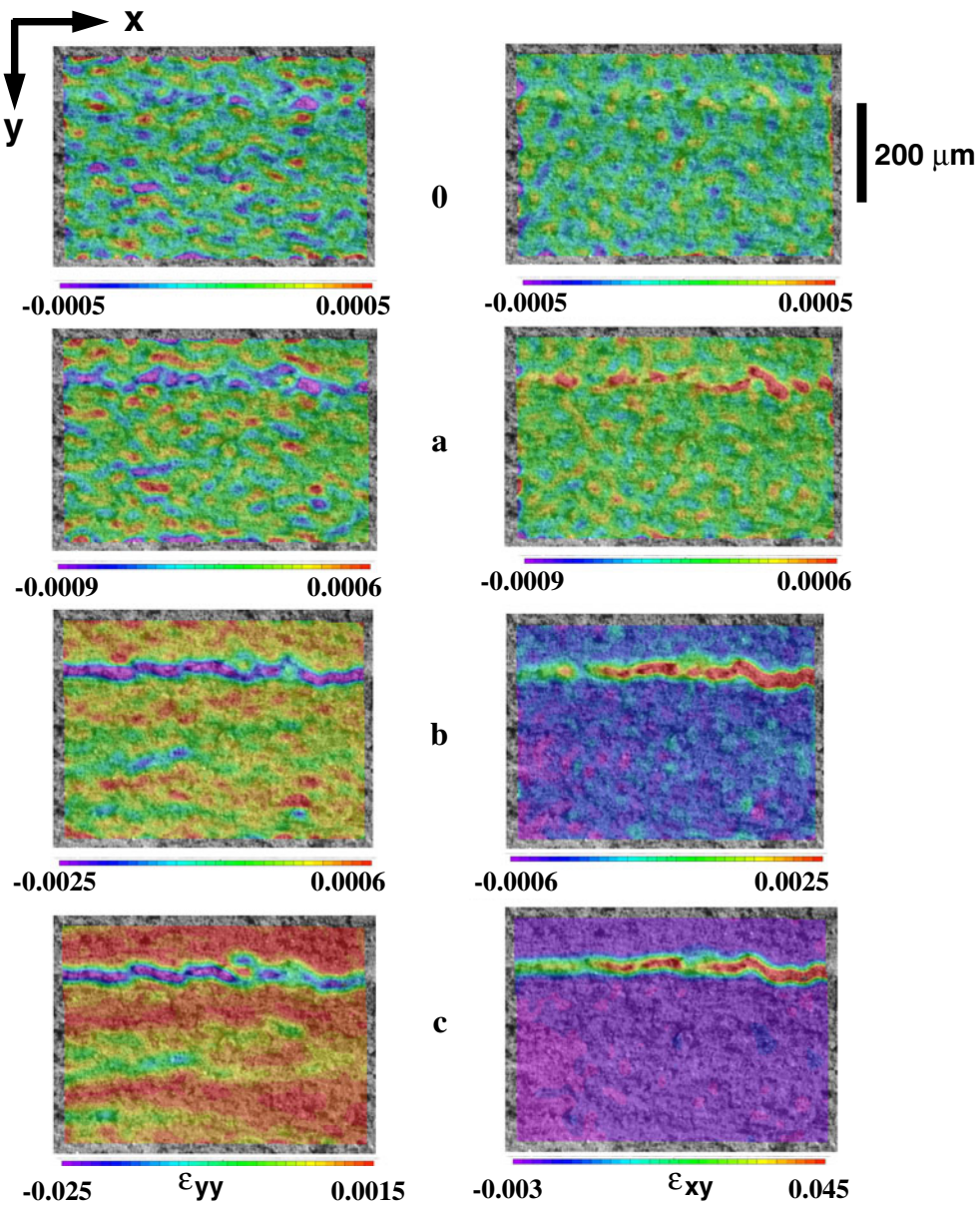

Fig. 12 Evolution of shear cracking in cellulose material. The pores collapse (**0**) and coalesce together (**a**) and accumulate shear strain (**b**) leading to macro crack (**c**). The pore collapse mechanism helps for load absorption. The images correspond approximately to the points 0, A, B, C in Fig. 13 (**c**)

at rates similar to the macro-scale flexural strain after failure, and faster than the microscale axial strain, which was approximately half the rate of the macro-scale flexural strain. Therefore, the faster increase in transverse and shear strains is consistent with their dominance in failure initiation. Furthermore, the accumulation of microscale transverse strain is nearly identical in the compressive and tensile regions. Since this strain is compressive, it is responsible for the pore collapse mechanism and indicates that pore collapse is independent of the global bending state, most likely due to the local macro-fiber bending previously characterized in Fig. 9. The evolution of the microscale strain components at a different location on the image is shown in Fig. 13 (e). The microscale strain is shown to increase at slightly different rate than the previous location, with a change in sign for shear strain due to inhomogeneity of the specimen at the microscale.

The macroscopic shear strain before failure initiation has been measured to be approximately 2% at the failure initiation site (Fig. 4). However, microscale pre-failure shear strain (in pore collapse) is determined to be as high as 4.5% (Fig. 12). These shear strain magnitudes are plausible given the hierarchical and inhomogeneous structure of the material at multiple length scales. Since a significant accumulation of strain at the microscale is required to initiate macroscopic failure, the macroscopic stress is limited by the level of microscale strain. Due to the compliance of the cellulose matrix, the micro-scale strain is not completely transferred to the higher length scale. The collapse of the cellulose matrix helps it to "absorb" strain locally and redistribute it to

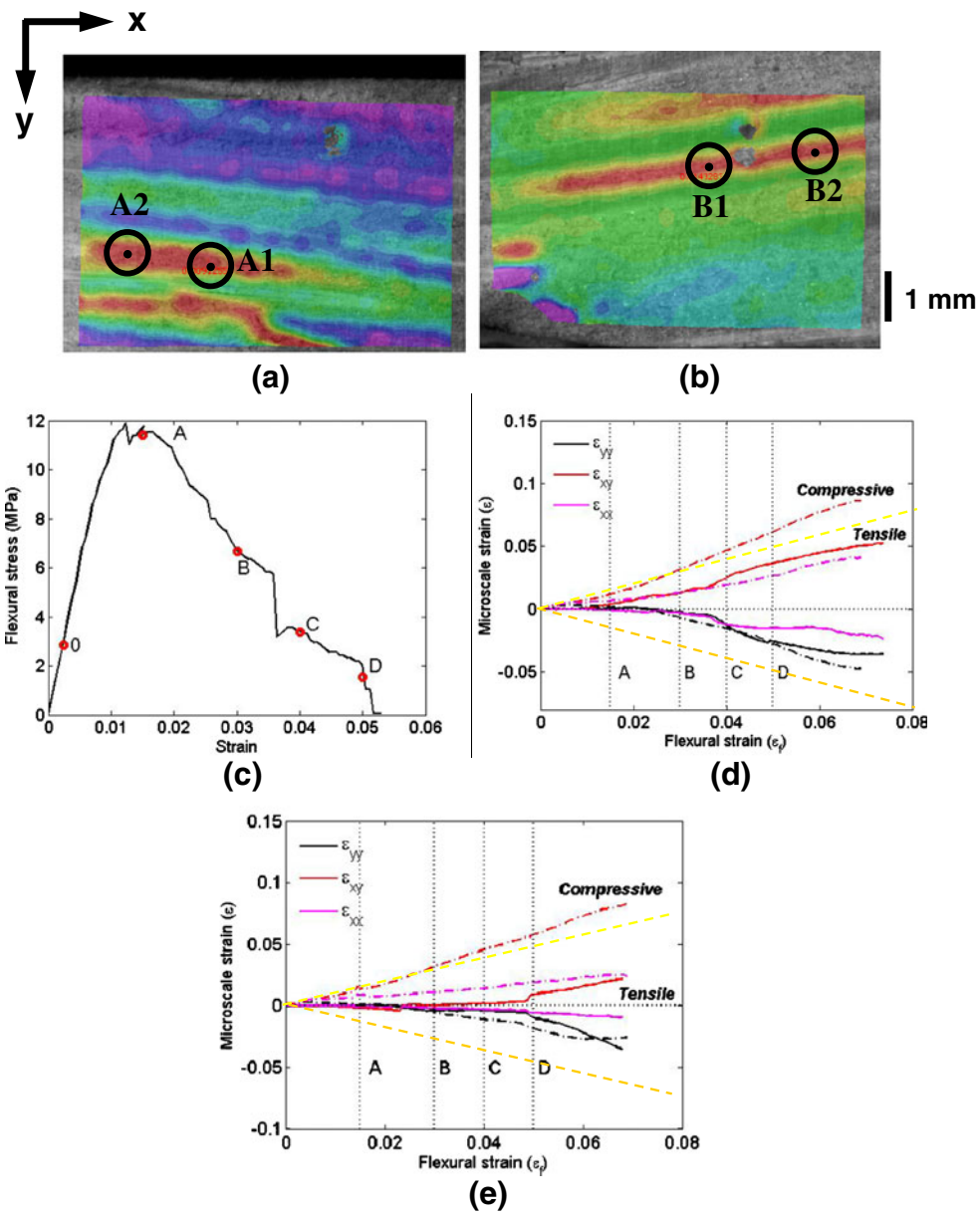

Fig. 13 Intermediate microscale shear strain field of interfiber matrix in (**a**) tensile and (**b**) compressive regions of the specimen, (**c**) macroscopic stress-strain response, and (**d**) the evolution of the microscale strains with macro-scale flexural strain (*right side*) in the tensile (*solid line*) and compressive (*dashed line*) regions. The strains were extracted at the encircled points A1, B1 in (**a**) and (**b**). The state of deformation corresponding to the points A, B, C and D are shown in the stress-strain response 1:1 correspondence between the magnitudes of the microscale strains and macro-scale flexural strain is denoted by the dashed yellow lines, (**e**) slightly different evolution of the strain components at different locations (A2, B2 in (**a**) and (**b**)) in the same image due to inhomogeneity

impede the initiation of macroscopic failure of the material. As discussed earlier, the porous media is weaker as opposed to the fiber material and does not transfer strain completely to the fiber. The matrix material absorbs the strain, requiring higher strain levels for macroscopic failure to initiate even though microscale failure may initiate earlier, which means microscale failure is actually initiating in the elastic regime at the macroscale.

Discussion of Results

DIC analysis has been performed at multiple length scales to understand the failure mechanism in Palmetto wood under three-point bending with quasi-static load. Several possible modes of failure are: (i) tensile failure on the tension side, (ii) buckling (wrinkling) on compression side or (iii) inter-layer delamination due to shear. Multiple length scale deformation measurements are performed under quasi-static load. Two types of cracking are noted in the specimens, namely macro-fiber-matrix debonding and matrix shear cracking. Both types of responses are found to be dominated by interlayer shear and transverse compression.

At the macro-scale, specimens prepared from the Palmetto wood exhibit more homogeneous material behavior as evidenced by homogeneous strain fields. The macro-scale bending can be mapped to that of a homogeneous isotropic material. However, highly inhomogeneous deformations due to the fiber reinforcement and matrix response can be distinguished at the microscale. The

periodicity of fiber and matrix is evident from the periodic nature of the shear strain distribution along the depth in specimen. High shear strain is found at the macro-fiber-matrix interfaces on both the globally tensile and globally compressive sides of the specimen. The fiber, being mechanically superior, does not deform as a porous matrix material (as expected), giving rise to shear strain concentrations at the fiber-matrix interface.

When obtaining microscale deformation measurement, the macro-fiber level has been noted to deform like a beam embedded in a compliant matrix giving rise to a classical bending profile. The compressive load is not transferred to the fiber since the inter-fiber matrix absorbs the load through a collapse mechanism. For this reason, crushing of the material at the loading point does not affect the far-field behavior of the specimen, and also enables the material to sustain higher normal load in the direction perpendicular to fiber alignment.

The tensile load is primarily carried by the fibers. Since the fibers are both stronger and more rigid than the surrounding matrix, the tensile region deforms less than the compressive zone. Failure at both the macro-fiber-matrix interface and cellulose matrix is seen to be dominated by interlayer debonding due to shear strain. The wavy nature of shear strain across the width of the specimen indicates high shear in the macro-fiber-matrix interface. The shear strain at potential failure sites appears to increase steadily until failure. Strain at the microscale is seen to be higher than measured at the macro-scale. This difference is acceptable at the microscale since local failure initiation does not immediately lead to macroscopic failure of the specimen because of local redistribution of the load within the multiple-laminate nature of wood.

Damage in the Palmetto wood material occurs via a multi-step failure process. The difference in mechanical properties between the compliant matrix and comparatively rigid macro-fibers results in high shear strain concentration at the interface. At the highest magnification scale, the pore collapse mechanism and accumulation of strain by pore collapse is observed. The shear cracking is noted to be initiated by the pore collapse at sites undergoing high shear strain and compressive strain. From the analysis of damage evolution for this material, the experimental measurement of the degraded modulus with elastic curvature shows a substantial initial drop. After the initial drop, the response does follow the upper bound for constant stress, indicating large initial load shedding consistent with macroscale failure followed by a more gradual evolution in microscale damage. From the damage evolution based on the hypothesis of elastic energy equivalence, it appears that the acceleration factor is quite high, indicating a rapid accumulation of microscale damage with strain throughout the Palmetto wood.

Conclusions

Mechanical characterization of Palmetto wood, a hierarchically structured natural material that can serve as a template for biologically-inspired polymer composites, has been investigated at multiple length scales using quasi-static three-point bend testing with the neutral axis of the specimen along the fiber orientation. Strain fields were determined at the various length scales using DIC across a range of optical magnifications in order to elucidate on the distinct roles of the porous cellulose matrix and embedded fibers in the failure process. The natural texture of the specimens was found to be adequate for image correlation across the length scales of interest.

It was determined from the quasi-static DIC results at the macro-scale that the material behaves fairly homogeneously with a slight asymmetry due to the presence of fibers. The macro-scale bending behavior complies well with the classical beam bending theory. However, microscale measurements at a magnification difference of 10X-20X relative to the macro-scale revealed inhomogeneous deformations due to differences in the properties of the macro-fibers and porous cellulose matrix. The shear and transverse strains exhibited significantly greater variability than the axial strain. The variability in shear strain coincided with debonding at the fiber-matrix interface or cracking within the matrix due to shear strain. The variability in transverse strain was primarily within the matrix and coincided with pore collapse.

It is postulated that the pore collapse mechanism acts as a load absorber that significantly reduces the energy available for fiber-matrix debonding, and enables the flexural response to translate from the macro-scale to the microscale in the macro-fiber. DIC measurements obtained at the highest magnification revealed that there was no further elucidation that could be obtained for the load transfer mechanism. However, the pore collapse mechanism and shear strain accumulation is elucidated. The microscale transverse normal strain and shear strains monotonically increase along with the macro-scale flexural strain at a faster rate than the longitudinal strain, indicating their dominance in the failure process. The microscale mechanical behavior was consistent in both the compression and tension regions of the three-point bend specimen, indicating that the failure process was not sensitive to the sign of the stress state.

Acknowledgements The financial support of Sandia National Laboratory through Sandia Contract PO#551836 and the support of Dr. Bruce LaMattina through ARO# W911NF-06-1-0216 and Dr. Yapa Rajapakse through ONR# N000140910640 are gratefully acknowledged. In addition, the research support provided by the Department of Mechanical Engineering at the University of South Carolina is also gratefully acknowledged.

References

1. Bruck HA, Evans JJ, Peterson ML (2002) The role of mechanics in biological and biologically inspired materials. Exp Mech 42 (4):361–371
2. Forsberg F, Sjodahl M, Mooser R, Hack E, Wyss P (2010) Full three-dimensional strain measurements on wood exposed to three-point bending: analysis by use of digital volume correlation applied to synchrotron radiation micro-computed tomography image data. Strain 46(1):47–60
3. Gershon AL, Bruck HA, Xu S, Sutton MA, Tiwari V (2010) Multiscale mechanical and structural characterizations of Palmetto wood for bio-inspired hierarchically structured polymer composites. Mater Sci Eng C 30:235–244
4. Wei A, Carlsson TE (2003) Speckle interferometry for measurement of continuous deformations. Opt Lasers Eng 40:529–541
5. Li X, Wei C, Yang Y (2005) Full field and microregion deformation measurement of thin films using electronic speckle pattern interferometry and array microindentation marker method. Opt Lasers Eng 43:869–884
6. Sutton MA, Mingqi C, Peters WH, Chao YJ, McNeill SR (1986) Application of an optimized digital correlation method to planar deformation analysis. Image Vis Comput 4:143–150
7. Czarnek R, Lee J, Rantis T (1990) Moiré interferometry with enhanced resolution. Exp Tech 2:24–8
8. Miller M, Mohammed L, Ho P (2001) Quantitative strain analysis of flip-chip electronic packages using phase-shifting moiré interferometry. Opt Lasers Eng 36:127–39
9. Morimoto Y, Hayashi T (1984) Deformation measurement during powder compaction by a scanning moiré method. Exp Mech 24:112–116
10. Chen H, Liu D, Lee A (2000) Moiré in atomic force microscope. Exp Tech 24(1):31–32
11. Chien CH, Wu YD, Chiou YT, Hsieh CC, Chen YC, Chen TP, Tsai ML, Wang CT (2006) Nanoscale deformation measurement by using the hybrid method of gray-level and holographic interferometry. Opt Lasers Eng 44:80–91
12. Chang M, Hu CP, Lam P, Wyant JC (1985) High precision deformation measurement by digital phase shifting holographic interferometry. Appl Opt 24(22):3780–3783
13. Creath K (1985) Phase-shifting speckle interferometry. Appl Opt 24(18):3053–3058
14. Pedrini G, Tiziani HJ (1994) Double-pulse electronic speckle interferometry for vibration analysis. Appl Opt 33(34):7857–63
15. Moore AJ, Hand DP, Barton JS, Jones JDC (1999) Transient deformation measurement with electronic speckle pattern interferometry and a high-speed camera. Optical Society of America 38:1159–1162
16. Anderson DJ, Valera JD, Jones JDC (1993) Electronic speckle pattern interferometry using diode laser spectroscopic illumination. Meas Sci Technol 4:982–987
17. Cookson TJ, Butters JN, Pollard HC (1978) Pulsed lasers in electronic speckle pattern interferometry. Opt Laser Technol 10:119–124
18. Moore AJ, Pérez-López C (1996) Fringe-visibility enhancement and phase calculation in double-pulsed addition ESPI. J Mod Opt 43:1829–1844
19. Zhang D, Arola DD (2004) Applications of digital image correlation to biological tissues. J Biomed Opt 9(4):691–699
20. Parks VJ (1982) Strain measurement using grids. Opt Eng 21:633–9
21. Goldrein HT, Palmer SJP, Huntley JM (1995) Automated fine grid technique for measurement of large-strain deformation maps. Opt Lasers Eng 23:305–18
22. Peters WH, Ranson WF (1981) Digital imaging techniques in experimental stress analysis. Opt Eng 21:427–31
23. Chu TC, Ranson WF, Sutton MA (1985) Applications of digital-image-correlation techniques to experimental mechanics. Exp Mech 25(3):232–44
24. Berfield TA, Patel JK, Shimmin RG, Braun PV, Lambros J, Sottos NR (2007) Micro- and nanoscale deformation measurement of surface and internalpPlanes via digital image correlation. Exp Mech 47:51–62
25. Davea S, Songa X, Hofmanna F, Dragnevskia K, Korsunsky AM (2009) Digital image correlation and finite element analysis of inter- and intra-granular deformation. Procedia Eng 1:197–200
26. Sztefek P, Vanleene M, Olsson R, Collinson R, Pitsillides AA, Shefelbine S (2009) Using digital image correlation to determine bone surface strains during loading and after adaptation of the mouse tibia. J Biomech. doi:10.1016/j.jbiomech.2009.10.042
27. Gonzalez J, Knauss WG (1998) Strain inhomogeneity and discontinuous crack growth in particulate composite. J Mech Phys Solids 35(09):1981–1985
28. Choi S, Shah SP (1997) Measurement of deformations on concrete subjected to compression using image correlation. Exp Mech 37(3):307–313
29. Wang Y, Cuitiño AM (2002) Full-field measurements of heterogeneous deformation patterns on polymeric foams using digital image correlation. Int J Solids Struct 39(13–14):3777–3796
30. Tong W (1997) Detection of plastic deformation patterns in a binary aluminum alloy. Exp Mech 37(4):452–459
31. Bastawros AF, Bart-Smith H, Evans AG (2000) Experimental analysis of deformation mechanisms in a closed-cell aluminum alloy foam. J Mech Phys Solids 48(2):301–322
32. Zink AG, Davidson RW, Hanna RB (1995) Strain measurement in wood using a digital image correlation technique. Wood Fiber Sci 27(4):346–359
33. Samarasinghe S, Kulasiri D, Nicolle K (1997) Study of mode-I and mixed-mode fracture in wood using digital image correlation method. Proceedings of International Wood Engineering Conference, Louisiana, USA
34. Chow CL, Lu TJ (1989) On evolution law of anisotropic damage. Eng Fract Mech 34(3):679–701